УДК 621.372.851

Electromagnetic Analysis of an Inductive Iris in a Rectangular Waveguide via a Hybrid Mode-Matching and Integral Equation Technique

Piltyay S. I.

National Technical University of Ukraine "Igor Sikorsky Kyiv Polytechnic Institute", Kyiv, Ukraine

E-mail: *s.piltiai@kpi.ua*

Inductive irises are applied in modern microwave filters, diplexers, polarizers, and rotators based on waveguides. The article presents an efficient mathematical technique for the analysis of the characteristics of the electromagnetic waves scattered by an inductive iris in a rectangular waveguide. Using the mode-matching technique for the transverse field components, the electromagnetic waves scattering problem was reduced to a set of coupled integral equations, which were then decoupled. Each equation was solved by expanding the electric field in the iris window into a series of basis functions. This procedure was implemented using sets of orthogonal trigonometric basis functions of the aperture field, orthogonal basis functions based on Gegenbauer polynomials with a weighting function of power 1/2, or orthogonal basis functions based on Gegenbauer polynomials with a weighting function of power 2/3. As a result, it became possible to determine the phasors of all modes in each region of the inner volume (before the iris, inside its aperture, and after the iris), along with the complex reflection and transmission coefficients of the fundamental electromagnetic mode TE_{10}. In order to validate the correctness and accuracy of the developed mathematical model, additional calculations by efficient numerical methods (Finite Element Method and Finite-Difference Time-Domain method) and experimental measurements of reflection characteristics were performed for two inductive irises in a standard rectangular waveguide. Measurement setups included a scalar network analyzer or a vector network analyzer, one of two inductive irises, a matching load, and waveguide channels. The experimentally obtained reflection coefficients were in good agreement with those predicted by the developed mathematical model and numerical methods. The developed mathematical model can be widely applied to the analysis of electromagnetic wave scattering by inductive irises in waveguides and to the synthesis of various microwave devices based on these irises.

Keywords: electromagnetic analysis; electromagnetic modeling; mode-matching technique; integral equations; inductive irises; rectangular waveguide; field distribution; basis functions; Gegenbauer polynomials; waveguide components

DOI: 10.64915/RADAP.2026.103.5-15

Introduction

Waveguide filters, polarizers, and other microwave devices often incorporate various types of inhomogeneous elements or discontinuities. Among these, the inductive iris is a reliable and easy-to-manufacture component [1–3]. The use of waveguide transmission lines for electromagnetic wave propagation ensures high efficiency, high power-handling capability, and low noise levels at microwave frequencies. This leads to the widespread utilization of various waveguide components for filtering [4, 5], diplexing [3, 6], and polarization processing [7, 8] in antenna systems for radar, satellite, and terrestrial telecommunications.

Various signal processing operations require specific components within waveguide transmission paths. Common functions include energy transfer to coupled waveguides, redirection of propagation, division or summation of power flows, and other linear operations. Directional couplers are employed to branch part of the power into auxiliary waveguides [9, 10]. Waveguide bends are effectively used to change the propagation direction, typically by 90° [11]. Power division and summation are implemented using E- or H-plane waveguide tees [12] and magic-T junctions [13]. Single-mode analysis of such devices can be performed using characteristic impedance concepts, equivalent network methods, and wave matrix techniques [14]. However, to achieve high accuracy in wideband applications, it is essential to employ rigorous full-wave numerical methods that account for higher-order mode interactions at waveguide discontinuities.

More complicated operations with electromagnetic modes in waveguides need the application of longi-

tudinally short components, near which concentration of electric or magnetic energy occurs. Mentioned operations include partial reflection of electromagnetic waves at specified frequencies, introduction of additional phase shifts, rotation of the polarization plane or transformation of the polarization type [15]. Waveguide devices for indicated processing include conducting irises [16], ridges [17,18], posts [19], and septa [20,21]. In the microwave frequency range highly accurate analysis of these lumped-type or inhomogeneous components can't be carried out by known circuit theory methods, which are effectively applied for calculating characteristics of components at lower frequencies.

Among all inhomogeneous waveguide components, the conducting iris has become widespread and critically important due to its versatility in simultaneously and effectively modifying the magnitude and phase of the electromagnetic waves, as well as its precise manufacturability using modern CPU-controlled milling machines. For these reasons, conducting irises are key elements of many state-of-the-art waveguide filters, polarizers, rotators [22–27].

At the same time, thin conducting irises have sharp edges with singular behavior of electromagnetic fields [28–31]. This leads to situations, when numerical software tools (CST Microwave Studio, Ansoft HFSS, etc.) for electromagnetic analysis can calculate characteristics less accurately or require more calculation time compared to rigorous theoretical approaches based on mode matching technique and the integral equations method. The proper selection of basis functions for decomposing the field distribution within the iris window can enhance the accuracy of the numerical method and ensure rapid convergence of the results.

Consequently, the development of a new, highly accurate analytical mathematical model of conducting irises in waveguides remains a relevant problem in modern electromagnetic theory. In addition, the question of choosing the best types of orthogonal basis functions for field decomposition in the window of an iris also requires clarification.

1 Research Objectives and Problem Statement

The purpose of this research is to develop a highly accurate mathematical model for electromagnetic wave scattering by a symmetric inductive iris in a rectangular waveguide. The proposed model must ensure high accuracy in calculating reflection and transmission coefficients, as well as phasors of the fundamental TE_{10} mode and higher-order modes. To achieve this objective, the following problems must be solved:

1) Deriving integral equations for the transverse electric (or magnetic) field distributions at the iris apertures using the mode-matching technique;
2) Linearizing the obtained integral equations via the Galerkin method;
3) Expanding the electric field in the window of a symmetric inductive iris using various sets of orthogonal basis functions.

2 Model of Electromagnetic Waves Propagation Through a Symmetric Inductive Iris in a Rectangular Waveguide

The segment of a rectangular waveguide containing a symmetric inductive iris is shown in Fig. 1. Designations of all inner dimensions are also presented in Fig. 2. Transverse inner sizes of the rectangular waveguide are $a \times b$. The width of the iris window is d, and its thickness is L.

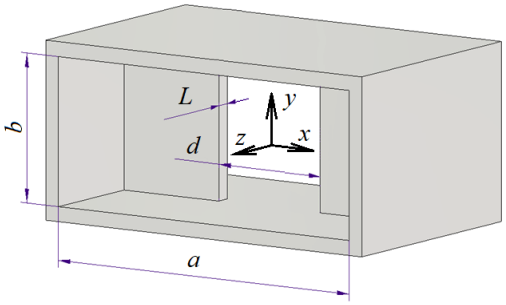

Fig. 1. Segment of a rectangular waveguide with a symmetric inductive iris and designations of the sizes

For the creation of the mathematical model, the total inner volume of the waveguide with a symmetric iris is divided into three parts. Volume decomposition is presented in Fig. 2.

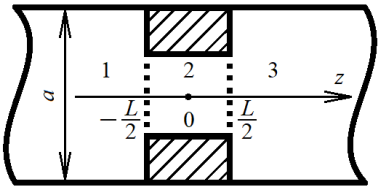

Fig. 2. Decomposition of the inner volume of a rectangular waveguide with an iris of thickness L

In volumes (1), (3) adjacent to the iris, and in the inner region (2), the transverse components of electric and magnetic vector fields have phasors as follows:

$$E_y^{(1)} = \dot{A}_1 \left(e^{-i\beta_1\left(z+\frac{L}{2}\right)} + \dot{\Gamma} e^{i\beta_1\left(z+\frac{L}{2}\right)} \right) \Phi_1(x) + \\ + \sum_{m=2}^{\infty} \dot{A}_m \Phi_m(x) e^{-i\dot{k}_m\left(z+\frac{L}{2}\right)}; \qquad (1)$$

$$H_x^{(1)} = -\dot{A}_1 \dot{Y}_1 \left(e^{-i\beta_1\left(z+\frac{L}{2}\right)} - \dot{\Gamma} e^{i\beta_1\left(z+\frac{L}{2}\right)} \right) \Phi_1(x) + \\ + \sum_{m=2}^{\infty} \dot{A}_m \dot{Y}_m \Phi_m(x) e^{-i\dot{k}_m\left(z+\frac{L}{2}\right)}; \qquad (2)$$

$$E_y^{(2)} = \sum_{n=1}^{\infty}(\dot{B}_n e^{-i\dot{\kappa}_n z} + \dot{C}_n e^{i\dot{\kappa}_n z})\Psi_n(x); \quad (3)$$

$$H_x^{(2)} = -\sum_{n=1}^{\infty}\left(\dot{B}_n e^{-i\dot{\kappa}_n z} - \dot{C}_n e^{i\dot{\kappa}_n z}\right)\dot{V}_n\Psi_n(x); \quad (4)$$

$$E_y^{(3)} = \dot{A}_1\dot{T}e^{-i\beta_1\left(z-\frac{L}{2}\right)}\Phi_1(x) + \\ + \sum_{m=2}^{\infty}\dot{F}_m\Phi_m(x)e^{i\dot{k}_m\left(z-\frac{L}{2}\right)}; \quad (5)$$

$$H_x^{(3)} = -\dot{A}_1\dot{T}\dot{Y}_1 e^{-i\beta_1\left(z-\frac{L}{2}\right)}\Phi_1(x) - \\ - \sum_{m=2}^{\infty}\dot{F}_m\dot{Y}_m\Phi_m(x)e^{i\dot{k}_m\left(z-\frac{L}{2}\right)}; \quad (6)$$

where $\dot{A}_1$, $\dot{A}_m$, $\dot{B}_n$, $\dot{C}_n$, $\dot{F}_m$ designate complex amplitude coefficients of the fundamental and higher modes, respectively, i stands for an imaginary unit, β_1, $\dot{k}_m$, $\dot{\kappa}_n$ denote wave numbers of the corresponding modes, $\dot{\Gamma}$ and $\dot{T}$ are complex reflection and transmission coefficients of the electric field of the fundamental mode, respectively, $\Phi_1(x), \Phi_m(x), \Psi_n(x)$ designate orthogonal normalized basis functions for transverse electric field distributions, and $\dot{Y}_1, \dot{Y}_m, \dot{V}_n$ are complex wave admittances that connect phasors of transverse magnetic and electric fields for each mode in a waveguide.

Helmholtz equations and boundary conditions at perfectly conducting walls are simultaneously satisfied by cosine basis functions of the following form:

$$\Phi_m(x) = \sqrt{\frac{2}{a}}\cos\left(\frac{(2m-1)\pi x}{a}\right), |x| \le a/2; \quad (7)$$

$$\Psi_n(x) = \begin{cases}\sqrt{\frac{2}{d}}\cos\left(\frac{(2n-1)\pi x}{d}\right), & |x| \le d/2 \\ 0, & d/2 \le |x| \le a/2\end{cases}. \quad (8)$$

Defined mathematical formulas (7), (8) of the basis functions allow one to obtain expressions for the remaining non-amplitude parameters of electromagnetic modes as follows:

$$\beta_1 = k_0\sqrt{1-\left(\frac{\pi}{k_0 a}\right)^2};$$

$$\dot{Y}_1 = \frac{\sqrt{1-\left(\frac{\pi}{k_0 a}\right)^2}}{Z_0};$$

$$\dot{k}_m = k_0\sqrt{1-\left(\frac{(2m-1)\pi}{k_0 a}\right)^2};$$

$$\dot{Y}_m = \frac{\sqrt{1-\left(\frac{(2m-1)\pi}{k_0 a}\right)^2}}{Z_0};$$

$$\dot{\kappa}_n = k_0\sqrt{1-\left(\frac{(2n-1)\pi}{k_0 d}\right)^2};$$

$$\dot{V}_n = \frac{\sqrt{1-\left(\frac{(2n-1)\pi}{k_0 d}\right)^2}}{Z_0},$$

where k_0 and Z_0 are the wave number and wave impedance of the material inside a rectangular waveguide.

In the next step, we match transverse electric fields from (1), (3) and transverse magnetic fields from (2), (4) on the first aperture plane ($z = -L/2$; $|x| \le d/2$). Simultaneously, the transverse electric fields of (3), (5) and the transverse magnetic fields from (4), (6) must be matched on the second aperture plane ($z = L/2$; $|x| \le d/2$). As a result, the following set of equations (9) is obtained. In addition, having designated transverse electric field distributions along the x axis on two iris apertures ($z = -L/2$ and $z = L/2$) as $\dot{E}_1(x)$ and $\dot{E}_2(x)$, we can write the set (10). After having projected (10) at basis functions $\Psi_n(x)$, we obtain the set of equations (11).

$$\begin{cases}\dot{A}_1(1+\dot{\Gamma})\Phi_1(x) + \sum\limits_{m=2}^{\infty}\dot{A}_m\Phi_m(x) = \sum\limits_{n=1}^{\infty}\left(\dot{B}_n e^{i\dot{\kappa}_n L/2} + \dot{C}_n e^{-i\dot{\kappa}_n L/2}\right)\Psi_n(x); \\ \dot{A}_1\dot{Y}_1(1-\dot{\Gamma})\Phi_1(x) - \sum\limits_{m=2}^{\infty}\dot{A}_m\dot{Y}_m\Phi_m(x) = \sum\limits_{n=1}^{\infty}\left(\dot{B}_n e^{i\dot{\kappa}_n L/2} - \dot{C}_n e^{-i\dot{\kappa}_n L/2}\right)\dot{V}_n\Psi_n(x); \\ \dot{A}_1\dot{T}\Phi_1(x) + \sum\limits_{m=2}^{\infty}\dot{F}_m\Phi_m(x) = \sum\limits_{n=1}^{\infty}\left(\dot{B}_n e^{-i\dot{\kappa}_n L/2} + \dot{C}_n e^{i\dot{\kappa}_n L/2}\right)\Psi_n(x); \\ \dot{A}_1\dot{T}\dot{Y}_1\Phi_1(x) + \sum\limits_{m=2}^{\infty}\dot{F}_m\dot{Y}_m\Phi_m(x) = \sum\limits_{n=1}^{\infty}\left(\dot{B}_n e^{-i\dot{\kappa}_n L/2} - \dot{C}_n e^{i\dot{\kappa}_n L/2}\right)\dot{V}_n\Psi_n(x).\end{cases} \quad (9)$$

$$\begin{cases}\sum\limits_{n=1}^{\infty}\left(\dot{B}_n e^{i\dot{k}_n L/2} + \dot{C}_n e^{-i\dot{k}_n L/2}\right)\Psi_n(x) = \dot{E}_1(x); \\ \sum\limits_{n=1}^{\infty}\left(\dot{B}_n e^{-i\dot{k}_n L/2} + \dot{C}_n e^{i\dot{k}_n L/2}\right)\Psi_n(x) = \dot{E}_2(x).\end{cases} \quad (10)$$

$$\begin{cases}\dot{B}_n e^{i\dot{\kappa}_n L/2} + \dot{C}_n e^{-i\dot{\kappa}_n L/2} = 2\int\limits_0^{d/2}\dot{E}_1(x)\Psi_n(x)\,dx; \\ \dot{B}_n e^{-i\dot{\kappa}_n L/2} + \dot{C}_n e^{i\dot{\kappa}_n L/2} = 2\int\limits_0^{d/2}\dot{E}_2(x)\Psi_n(x)\,dx.\end{cases} \quad (11)$$

The solution of the set of equations (11) is as follows:

$$\dot{B}_n = \frac{i\left(e^{-i\dot{\kappa}_n L/2}\int\limits_0^{d/2}\dot{E}_2(x)\Psi_n(x)\,dx - e^{i\dot{\kappa}_n L/2}\int\limits_0^{d/2}\dot{E}_1(x)\Psi_n(x)\,dx\right)}{\sin(\dot{\kappa}_n L)}; \tag{12}$$

$$\dot{C}_n = \frac{i\left(e^{-i\dot{\kappa}_n L/2}\int\limits_0^{d/2}\dot{E}_1(x)\Psi_n(x)\,dx - e^{i\dot{\kappa}_n L/2}\int\limits_0^{d/2}\dot{E}_2(x)\Psi_n(x)\,dx\right)}{\sin(\dot{\kappa}_n L)}. \tag{13}$$

Next, we substitute (10) and phasors (12), (13) in (9). These substitutions yield the set of equations (14):

$$\begin{cases} \dot{A}_1(1+\dot{\Gamma})\Phi_1(x) + \sum\limits_{m=2}^{\infty}\dot{A}_m\Phi_m(x) = \dot{E}_1(x); \\ \dot{A}_1\dot{Y}_1(1-\dot{\Gamma})\Phi_1(x) - \sum\limits_{m=2}^{\infty}\dot{A}_m\dot{Y}_m\Phi_m(x) = \\ = 2\sum\limits_{n=1}^{\infty}\left(\frac{\int\limits_0^{d/2}\left(\dot{E}_1(x)\cos(\dot{\kappa}_n L) - \dot{E}_2(x)\right)\Psi_n(x)\,dx}{i\sin(\dot{\kappa}_n L)}\right)\dot{V}_n\Psi_n(x); \\ \dot{A}_1\dot{T}\Phi_1(x) + \sum\limits_{m=2}^{\infty}\dot{F}_m\Phi_m(x) = \dot{E}_2(x); \\ \dot{A}_1\dot{T}\dot{Y}_1\Phi_1(x) + \sum\limits_{m=2}^{\infty}\dot{F}_m\dot{Y}_m\Phi_m(x) = \\ = 2\sum\limits_{n=1}^{\infty}\left(\frac{\int\limits_0^{d/2}\left(\dot{E}_1(x) - \dot{E}_2(x)\cos(\dot{\kappa}_n L)\right)\Psi_n(x)\,dx}{i\sin(\dot{\kappa}_n L)}\right)\dot{V}_n\Psi_n(x). \end{cases} \tag{14}$$

Let the complex amplitude coefficient of the fundamental mode $\dot{A}_1 = 1$. Then, the multiplication of the first equation of the set (14) by $\Phi_1(x)$ or $\Phi_m(x)$ and its subsequent integration over the orthogonality interval $(-a/2;\, a/2)$ allows one to express the complex reflection coefficient $\dot{\Gamma}$ and phasors $\dot{A}_m$ as follows:

$$\dot{\Gamma} = 2\int\limits_0^{d/2}\dot{E}_1(x)\Phi_1(x)\,dx - 1; \tag{15}$$

$$\dot{A}_m = 2\int\limits_0^{d/2}\dot{E}_1(x)\Phi_m(x)\,dx. \tag{16}$$

Having performed similar operations with the third equation of the set (14), we obtain expressions for the complex transmission coefficient $\dot{T}$ and the phasors $\dot{F}_m$ as follows:

$$\dot{T} = 2\int\limits_0^{d/2}\dot{E}_2(x)\Phi_1(x)\,dx; \tag{17}$$

$$\dot{F}_m = 2\int\limits_0^{d/2}\dot{E}_2(x)\Phi_m(x)\,dx. \tag{18}$$

Now, we substitute (15)–(18) into the second and fourth equations of the set (14), taking into account that $\dot{A}_1 = 1$. As a result, the following set of two coupled integral equations (19) is obtained for the sought transverse electric field distributions $\dot{E}_1(x)$ and $\dot{E}_2(x)$. This set can be decoupled into two independent integral equations. To this end, we add and subtract the equations in (19), which yields equations (20) and (21).

$$\begin{cases} \sum\limits_{n=1}^{\infty}\left(\frac{\int_0^{d/2}\left(\dot{E}_1(x)\cos(\dot{\kappa}_n L) - \dot{E}_2(x)\right)\Psi_n(x)dx}{i\sin(\dot{\kappa}_n L)}\right)\dot{V}_n\Psi_n(x) + \\ + \sum\limits_{m=1}^{\infty}\left(\int_0^{d/2}\dot{E}_1(x)\Phi_m(x)dx\right)\dot{Y}_m\Phi_m(x) = \dot{Y}_1\Phi_1(x); \\ \sum\limits_{n=1}^{\infty}\left(\frac{\int_0^{d/2}\left(\dot{E}_2(x)\cos(\dot{\kappa}_n L) - \dot{E}_1(x)\right)\Psi_n(x)dx}{i\sin(\dot{\kappa}_n L)}\right)\dot{V}_n\Psi_n(x) + \\ + \sum\limits_{m=1}^{\infty}\left(\int_0^{d/2}\dot{E}_2(x)\Phi_m(x)dx\right)\dot{Y}_m\Phi_m(x) = 0; \end{cases} \tag{19}$$

$$i\sum_{n=1}^{\infty}\left(\dot{V}_n\,\mathrm{tg}\left(\frac{\dot{\kappa}_n L}{2}\right)\Psi_n(x)\int_0^{d/2}\dot{E}_\Sigma(x)\Psi_n(x)dx\right) + \\ + \sum_{m=1}^{\infty}\left(\dot{Y}_m\Phi_m(x)\int_0^{d/2}\dot{E}_\Sigma(x)\Phi_m(x)dx\right) = \dot{Y}_1\Phi_1(x); \tag{20}$$

$$i\sum_{n=1}^{\infty}\left(\dot{V}_n\,\mathrm{ctg}\left(\frac{\dot{\kappa}_n L}{2}\right)\Psi_n(x)\int_0^{d/2}\dot{E}_\Delta(x)\Psi_n(x)dx\right) - \\ - \sum_{m=1}^{\infty}\left(\dot{Y}_m\Phi_m(x)\int_0^{d/2}\dot{E}_\Delta(x)\Phi_m(x)dx\right) = \dot{Y}_1\Phi_1(x), \tag{21}$$

where the sum and difference of the transverse electric field distributions are $\dot{E}_\Sigma(x) = \dot{E}_1(x) + \dot{E}_2(x)$ and $\dot{E}_\Delta(x) = \dot{E}_2(x) - \dot{E}_1(x)$, respectively.

Once the solutions $\dot{E}_\Sigma(x)$ and $\dot{E}_\Delta(x)$ to the integral equations (20) and (21) are found, the sought electric field distributions $\dot{E}_1(x)$ and $\dot{E}_2(x)$ are obtained as their half-difference and half-sum, respectively:

$$\dot{E}_1(x) = \frac{\dot{E}_\Sigma(x) - \dot{E}_\Delta(x)}{2}, \quad \dot{E}_2(x) = \frac{\dot{E}_\Sigma(x) + \dot{E}_\Delta(x)}{2}. \tag{22}$$

Subsequent substitution of $\dot{E}_1(x)$ and $\dot{E}_2(x)$ into (15)–(18) allows for finding the phasors of all modes in each region (before, inside and after the iris), as well as the complex reflection and transmission coefficients.

3 Aperture Transverse Electric Field Expansion via Trigonometric Functions and Weighted Gegenbauer Polynomials

To solve the integral equations, let us expand the unknown fields $\dot{E}_\Sigma(x)$ and $\dot{E}_\Delta(x)$ into a series of basis functions $R_j(x)$ that correctly account for the boundary conditions at the electric walls:

$$\dot{E}_\Sigma(x) = \sum_{j=1}^{\infty} \dot{s}_j R_j(x), \quad \dot{E}_\Delta(x) = \sum_{j=1}^{\infty} \dot{p}_j R_j(x), \quad (23)$$

where $\dot{s}_j$ and $\dot{p}_j$ are the unknown expansion coefficients. To simplify the evaluation of the integrals, we assume that these functions vanish outside the iris aperture: $R_j(x) = 0$ for $|x| \geq d/2$.

Substituting (23) into (20) and (21), we obtain the following equations:

$$i\sum_{j=1}^{\infty} \dot{s}_j \left[\sum_{n=1}^{\infty} \dot{V}_n \tan\left(\frac{\dot{\kappa}_n L}{2}\right) I_{R\Psi}(j,n)\Psi_n(x)\right] + \\ + \sum_{j=1}^{\infty} \dot{s}_j \left[\sum_{m=1}^{\infty} \dot{Y}_m I_{R\Phi}(j,m)\Phi_m(x)\right] = \dot{Y}_1\Phi_1(x), \quad (24)$$

$$i\sum_{j=1}^{\infty} \dot{p}_j \left[\sum_{n=1}^{\infty} \dot{V}_n \cot\left(\frac{\dot{\kappa}_n L}{2}\right) I_{R\Psi}(j,n)\Psi_n(x)\right] - \\ - \sum_{j=1}^{\infty} \dot{p}_j \left[\sum_{m=1}^{\infty} \dot{Y}_m I_{R\Phi}(j,m)\Phi_m(x)\right] = \dot{Y}_1\Phi_1(x), \quad (25)$$

where $I_{R\Psi}(j,n) = \int_0^{d/2} R_j(x)\Psi_n(x)\,dx$ and $I_{R\Phi}(j,m) = \int_0^{d/2} R_j(x)\Phi_m(x)\,dx$.

To transform the functional equations (24) and (25) into systems of linear algebraic equations (SLAEs), we project them onto the basis functions of the iris aperture. To this end, the equations are multiplied by $\Psi_k(x)$ and integrated over the orthogonality interval $(-d/2, d/2)$ with respect to the coordinate x. As a result, we obtain infinite-order SLAEs for the unknown complex expansion coefficients $\dot{s}_j$ and $\dot{p}_j$ as follows:

$$\sum_{j=1}^{\infty} \dot{s}_j \left[i\dot{V}_k \tan\left(\frac{\dot{\kappa}_k L}{2}\right) I_{R\Psi}(j,k) + \right. \\ \left. + \sum_{m=1}^{\infty} \dot{Y}_m I_{R\Phi}(j,m) I_{\Phi\Psi}(m,k)\right] = \dot{Y}_1 I_{\Phi\Psi}(1,k), \quad (26)$$
$$k = 1, 2, \ldots;$$

$$\sum_{j=1}^{\infty} \dot{p}_j \left[i\dot{V}_k \cot\left(\frac{\dot{\kappa}_k L}{2}\right) I_{R\Psi}(j,k) - \right. \\ \left. - \sum_{m=1}^{\infty} \dot{Y}_m I_{R\Phi}(j,m) I_{\Phi\Psi}(m,k)\right] = \dot{Y}_1 I_{\Phi\Psi}(1,k), \quad (27)$$
$$k = 1, 2, \ldots,$$

where $I_{\Phi\Psi}(m,n) = 2\int_0^{d/2} \Phi_m(x)\Psi_n(x)\,dx$ is the overlap integral:

$$I_{\Phi\Psi}(m,n) = \sqrt{\frac{d}{a}}\left[\operatorname{sinc}(\xi_+) + \operatorname{sinc}(\xi_-)\right],$$
$$\xi_\pm = \frac{\pi d}{2}\left(\frac{2m-1}{a} \pm \frac{2n-1}{d}\right),$$

and $\operatorname{sinc}(x) = \sin(x)/x$.

To solve SLAEs (26) and (27) numerically, they must be truncated to a finite order N, where N is the number of equations and unknown expansion coefficients $\dot{s}_j$ and $\dot{p}_j$. The convergence of the numerical solution is ensured by increasing N, with a relatively small number of terms typically required due to the rigorous treatment of the edge conditions. Once the coefficients are determined, they are substituted into (23) to obtain the sum and difference of the transverse electric field distributions. Finally, substituting $\dot{E}_\Sigma(x)$ and $\dot{E}_\Delta(x)$ into (22) yields the electric field distributions at both iris apertures:

$$\dot{E}_1(x) = \sum_{j=1}^{N} \frac{\dot{s}_j - \dot{p}_j}{2} R_j(x), \quad \dot{E}_2(x) = \sum_{j=1}^{N} \frac{\dot{s}_j + \dot{p}_j}{2} R_j(x). \quad (28)$$

Consequently, the reflection and transmission coefficients, as well as the phasors of higher-order modes, are calculated as follows:

$$\dot{\Gamma} = \sum_{j=1}^{N} (\dot{s}_j - \dot{p}_j) I_{R\Phi}(j,1) - 1,$$
$$\dot{T} = \sum_{j=1}^{N} (\dot{s}_j + \dot{p}_j) I_{R\Phi}(j,1),$$
$$\dot{A}_m = \sum_{j=1}^{N} (\dot{s}_j - \dot{p}_j) I_{R\Phi}(j,m),$$
$$\dot{F}_m = \sum_{j=1}^{N} (\dot{s}_j + \dot{p}_j) I_{R\Phi}(j,m).$$

The transverse electric field component is tangential to the sharp edges of the conducting iris in the rectangular waveguide (region 2 in Fig. 2). According to [30,31], for a thin iris, the behavior of the tangential electric field near the edge is as follows:

$$E_y\Big|_{x\to\pm d/2} \sim \left[1 - \left(\frac{2x}{d}\right)^2\right]^{1/2}.$$

In the case of a thick iris or a conducting step with angle 90°, the singular behavior of the electric field is different:

$$E_y\Big|_{x\to\pm d/2} \sim \left[1 - \left(\frac{2x}{d}\right)^2\right]^{2/3}.$$

These functional dependences determine the recommended forms of the basis functions $R_j(x)$. The

simplest variant of basis functions, which are equal to 0 at the electric walls of the iris, are the trigonometric functions, which coincide with the eigenfunctions of the solution of boundary problem:

$$R_j^{(1)}(x) = \begin{cases} \sqrt{\frac{2}{d}} \cos\left(\frac{(2j-1)\pi x}{d}\right), & |x| \le d/2 \\ 0, & d/2 \le |x| \le a/2. \end{cases} \tag{29}$$

For basis functions of this kind, the values of integrals $I_{R\Psi}(j,n)$ and $I_{R\Phi}(j,m)$ are as follows:

$$I_{\mathrm{R}\Psi}(j,n) = \int_0^{d/2} \Psi_j(x)\Psi_n(x)\,dx = \frac{\delta_{j,n}}{2};$$

$$I_{\mathrm{R}\Phi}(j,m) = \int_0^{d/2} \Psi_j(x)\Phi_m(x)\,dx = \frac{I_{\Phi\Psi}(m,j)}{2},$$

where $\delta_{j,n}$ stands for the Kronecker delta.

Mutually orthogonal (at interval $|x| \le d/2$) basis functions, which correctly take into account electric field behavior, are constructed as the product of the weighting function of power 1/2 or 2/3 and the even-order Gegenbauer polynomials [32, 33] with superscripts 3/2 or 11/6, respectively:

$$R_j^{(2)}(x) = \left[1 - \left(\frac{2x}{d}\right)^2\right]^{1/2} C_{2j-2}^{3/2}\left(\frac{2x}{d}\right); \tag{30}$$

$$R_j^{(3)}(x) = \left[1 - \left(\frac{2x}{d}\right)^2\right]^{2/3} C_{2j-2}^{11/6}\left(\frac{2x}{d}\right). \tag{31}$$

The functions (30) and (31) correspond to the singular behavior of the tangential electric field at the infinitely thin conducting half-plane and at the conducting right-angled wedge, respectively. Gegenbauer polynomials $C_n^{\alpha}\left(\frac{2x}{d}\right)$ can be expressed by the following recurrence relation:

$$C_0^{\alpha}\left(\frac{2x}{d}\right) = 1; \quad C_1^{\alpha}\left(\frac{2x}{d}\right) = 4\alpha\frac{x}{d};$$

$$C_{n+1}^{\alpha}\left(\frac{2x}{d}\right) = \frac{4(n+\alpha)\frac{x}{d}C_n^{\alpha}\left(\frac{2x}{d}\right)}{n+1} - \frac{(n+2\alpha-1)C_{n-1}^{\alpha}\left(\frac{2x}{d}\right)}{n+1}, \quad \text{for } n \in \mathbb{N},$$

where $\alpha = 3/2$ or 11/6 for the function (30) or (31), respectively.

Having substituted functions (29)–(31) into (28), we obtain explicit forms of decomposition of the transverse electric fields at both iris apertures:

$$E_1^{(1)}(x) = \begin{cases} \sum_{j=1}^{\infty} \frac{\dot{s}_j - \dot{p}_j}{\sqrt{2d}} \cos\frac{(2j-1)\pi x}{d}, & |x| \le d/2 \\ 0, & d/2 \le |x| \le a/2 \end{cases};$$

$$E_2^{(1)}(x) = \begin{cases} \sum_{j=1}^{\infty} \frac{\dot{s}_j + \dot{p}_j}{\sqrt{2d}} \cos\frac{(2j-1)\pi x}{d}, & |x| \le d/2 \\ 0, & d/2 \le |x| \le a/2 \end{cases};$$

$$E_1^{(2)}(x) = \sum_{j=1}^{\infty} \frac{\dot{s}_j - \dot{p}_j}{2}\left[1 - \left(\frac{2x}{d}\right)^2\right]^{1/2} C_{2j-2}^{3/2}\left(\frac{2x}{d}\right);$$

$$E_2^{(2)}(x) = \sum_{j=1}^{\infty} \frac{\dot{s}_j + \dot{p}_j}{2}\left[1 - \left(\frac{2x}{d}\right)^2\right]^{1/2} C_{2j-2}^{3/2}\left(\frac{2x}{d}\right);$$

$$\dot{E}_1^{(3)}(x) = \sum_{j=1}^{\infty} \frac{\dot{s}_j - \dot{p}_j}{2}\left[1 - \left(\frac{2x}{d}\right)^2\right]^{2/3} C_{2j-2}^{11/6}\left(\frac{2x}{d}\right);$$

$$\dot{E}_2^{(3)}(x) = \sum_{j=1}^{\infty} \frac{\dot{s}_j + \dot{p}_j}{2}\left[1 - \left(\frac{2x}{d}\right)^2\right]^{2/3} C_{2j-2}^{11/6}\left(\frac{2x}{d}\right).$$

A drawback of the introduced orthogonal basis functions (30), (31) is the lack of analytical solutions for the integrals $I_{R\Psi}(j,n)$ and $I_{R\Phi}(j,m)$ that arise in the applied mathematical method. Calculating these integrals is computationally intensive due to the numerical integration of products of the basis functions (30), (31) and the highly oscillatory higher-order eigenfunctions (7), (8).

4 Calculated and Measured Reflection Coefficients of Inductive Irises in a Waveguide

To validate the developed mathematical model, the frequency dependence of the reflection coefficients was first established through numerical methods (FEM and FDTD) and experimental measurements for two inductive irises in a rectangular waveguide. The experimental setup consisted of an Anritsu MS46122A vector network analyzer (VNA) or a scalar network analyzer (SNA), one of the two inductive irises, a matched load and waveguide sections with an inner cross-section of 23×10 mm^2. The equipment used in the experiments is shown in Fig. 3.

Two thin inductive irises, which were investigated using setups, are demonstrated in Fig. 4. Each iris was placed at the end of the waveguide transmission channel before the matching load in the setup shown in Fig. 3a and between the waveguide flanges in the setup shown in Fig. 3b. The inner dimensions of the irises, which were applied in the experiments, are presented in Table 1.

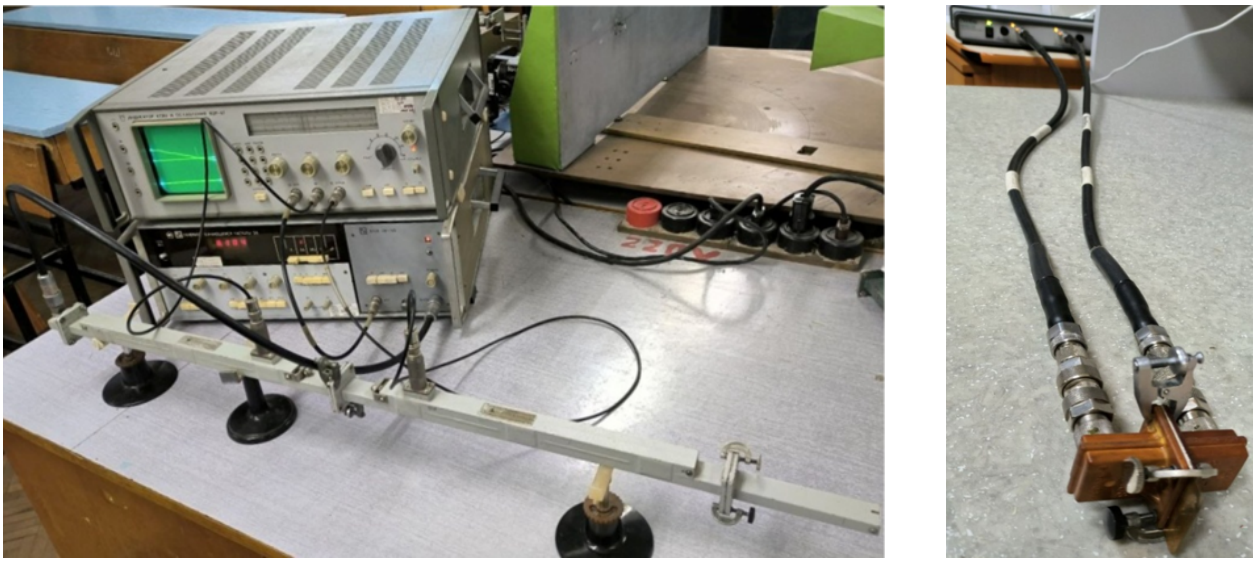

(a) (b)

Fig. 3. Setups for measurement of the reflection coefficient of the electromagnetic waves scattered by an iris in a rectangular waveguide using: (a) scalar network analyzer; (b) vector network analyzer

Fig. 4. Inductive irises used in measurements

The magnitudes and phases of the reflection coefficients, obtained via measurements and numerical simulations (FEM and FDTD), are presented in Tables 2 and 3 for irises 1 and 2, respectively. Deviations between measured and calculated values stem from experimental uncertainties, including setup calibration inaccuracies and fabrication tolerances. Additional errors are introduced by angular alignment offsets and imperfect flange contacts. The discrepancies between the measured and simulated magnitudes do not exceed 1.3dB for iris 1 and 0.9dB for iris 2, while the phase differences remain below 4° and 2.5°, respectively.

Consequently, a satisfactory agreement between the numerical and experimental results is observed across the investigated frequency range. Nevertheless, the FEM and FDTD results differ slightly. Recent studies confirm that the FEM remains the preferred tool for modeling electromagnetic field singularities at sharp metallic discontinuities [34,35]. Its adaptive mesh refinement allows for a more rigorous characterization of edge effects compared to the FDTD method, which is often limited by staircasing errors. Given the aforementioned experimental uncertainties, the FEM results will be used as a reference to validate the developed mathematical model and the three types of basis functions (BFs) (29)–(31).

The calculated reflection coefficients, obtained using the FEM and the proposed mathematical model with different BFs, are presented in Tables 4 and 5. These values were calculated using 200 BFs (29), 10 BFs (30) and (31), and by including up to 200 terms in the infinite sums (26) and (27).

The comparative analysis of the results in Tables 4 and 5 confirms the high accuracy of the developed model. A detailed examination indicates that BFs (31) provide the closest agreement with the FEM results for both irises. Specifically, the maximum magnitude deviation for BFs (31) does not exceed 0.011dB for iris 1 and 0.009dB for iris 2, while the maximum phase deviation is below 0.03° for both irises. Therefore, BFs (31) are optimal for the analyzed structures.

Table 1 Inner dimensions of the investigated inductive irises in a 23×10 mm^2 rectangular waveguide

A variant of an inductive iris	1	2
Dimension	Absolute value, mm (relative value with respect to width a)	Absolute value, mm (relative value with respect to width a)
Window width, d	17.0 ($0.739a$)	16.2 ($0.704a$)
Window height, b	10.0 ($0.435a$)	10.0 ($0.435a$)
Iris thickness, L	0.14 ($0.00609a$)	0.50 ($0.0217a$)

Table 2 Magnitudes and phases of the reflection coefficient for inductive iris 1

Frequency, GHz	Measured by SNA $\lvert S_{1,1}\rvert$, (dB)	Measured by VNA $\lvert S_{1,1}\rvert$, (dB)	Calculated by FDTD $\lvert S_{1,1}\rvert$, (dB)	Calculated by FEM $\lvert S_{1,1}\rvert$, (dB)	Measured by VNA Phase of $S_{1,1}$, (deg)	Calculated by FDTD Phase of $S_{1,1}$, (deg)	Calculated by FEM Phase of $S_{1,1}$, (deg)
8.0	−10.7	−10.8	−11.55	−11.527	106.6	103.6	104.63
8.5	−12.4	−12.1	−12.91	−12.914	104.4	102.7	102.18
9.0	−12.8	−13.3	−14.02	−14.053	101.3	100.2	100.43
9.5	−13.8	−14.3	−15.04	−15.032	100.1	99.2	99.08
10.0	−16.2	−15.2	−15.87	−15.900	98.0	97.9	97.99
10.5	−16.8	−16.0	−16.69	−16.688	96.6	97.2	97.08
11.0	−17.4	−16.9	−17.37	−17.416	95.7	96.2	96.30
11.5	−18.2	−17.7	−18.12	−18.099	94.7	95.7	95.61
12.0	−19.0	−18.7	−18.68	−18.747	94.6	94.8	94.99
12.5	−19.9	−19.0	−19.45	−19.369	90.8	94.7	94.44

Table 3 Magnitudes and phases of the reflection coefficient for inductive iris 2

Frequency, GHz	Measured by SNA $\lvert S_{1,1}\rvert$, (dB)	Measured by VNA $\lvert S_{1,1}\rvert$, (dB)	Calculated by FDTD $\lvert S_{1,1}\rvert$, (dB)	Calculated by FEM $\lvert S_{1,1}\rvert$, (dB)	Measured by VNA Phase of $S_{1,1}$, (deg)	Calculated by FDTD Phase of $S_{1,1}$, (deg)	Calculated by FEM Phase of $S_{1,1}$, (deg)
8.0	−7.9	−8.4	−8.34	−8.320	110.1	109.2	109.93
8.5	−9.6	−9.7	−9.61	−9.631	107.5	106.5	106.17
9.0	−10.1	−10.9	−10.72	−10.733	104.8	103.2	103.38
9.5	−11.2	−11.8	−11.69	−11.697	103.1	101.3	101.15
10.0	−12.1	−12.6	−12.56	−12.566	101.2	99.2	99.31
10.5	−13.0	−13.4	−13.36	−13.364	99.4	97.8	97.72
11.0	−14.8	−14.2	−14.10	−14.111	98.0	96.2	96.33
11.5	−15.5	−15.0	−14.82	−14.819	97.2	95.2	95.08
12.0	−16.2	−15.7	−15.48	−15.498	96.2	93.7	93.95
12.5	−17.0	−16.0	−16.16	−16.158	95.2	93.2	92.90

Table 4 Calculated magnitudes and phases of the reflection coefficient for inductive iris 1

Frequency, GHz	Calculated by FEM $\lvert S_{1,1}\rvert$, (dB)	Calculated by Model & BFs (29) $\lvert S_{1,1}\rvert$, (dB)	Calculated by Model & BFs (30) $\lvert S_{1,1}\rvert$, (dB)	Calculated by Model & BFs (31) $\lvert S_{1,1}\rvert$, (dB)	Calculated by FEM Phase of $S_{1,1}$, (deg)	Calculated by Model & BFs (29) $\angle S_{1,1}$, (deg)	Calculated by Model & BFs (30) $\angle S_{1,1}$, (deg)	Calculated by Model & BFs (31) $\angle S_{1,1}$, (deg)
8.0	−11.527	−11.513	−11.556	−11.530	104.63	104.65	104.58	104.62
8.5	−12.914	−12.904	−12.947	−12.921	102.18	102.20	102.13	102.17
9.0	−14.053	−14.044	−14.088	−14.062	100.43	100.44	100.38	100.42
9.5	−15.032	−15.024	−15.068	−15.042	99.08	99.09	99.04	99.07
10.0	−15.900	−15.893	−15.937	−15.911	97.99	98.00	97.95	97.98
10.5	−16.688	−16.681	−16.725	−16.699	97.08	97.09	97.05	97.07
11.0	−17.416	−17.409	−17.453	−17.427	96.30	96.30	96.26	96.29
11.5	−18.099	−18.092	−18.136	−18.110	95.61	95.62	95.58	95.60
12.0	−18.747	−18.740	−18.784	−18.758	94.99	95.00	94.97	94.99
12.5	−19.369	−19.362	−19.405	−19.380	94.44	94.44	94.41	94.43

Table 5 Calculated magnitudes and phases of the reflection coefficient for inductive iris 2

Frequency, GHz	Calculated by FEM $\lvert S_{1,1}\rvert$, (dB)	Calculated by Model & BFs (29) $\lvert S_{1,1}\rvert$, (dB)	Calculated by Model & BFs (30) $\lvert S_{1,1}\rvert$, (dB)	Calculated by Model & BFs (31) $\lvert S_{1,1}\rvert$, (dB)	Calculated by FEM Phase of $S_{1,1}$, (deg)	Calculated by Model & BFs (29) $\angle S_{1,1}$, (deg)	Calculated by Model & BFs (30) $\angle S_{1,1}$, (deg)	Calculated by Model & BFs (31) $\angle S_{1,1}$, (deg)
8.0	−8.320	−8.307	−8.322	−8.311	109.93	109.97	109.93	109.96
8.5	−9.631	−9.620	−9.635	−9.624	106.17	106.20	106.17	106.19
9.0	−10.733	−10.723	−10.738	−10.728	103.38	103.40	103.37	103.39
9.5	−11.697	−11.689	−11.704	−11.693	101.15	101.18	101.15	101.17
10.0	−12.566	−12.557	−12.573	−12.562	99.31	99.33	99.30	99.32
10.5	−13.364	−13.356	−13.372	−13.361	97.72	97.74	97.72	97.74
11.0	−14.111	−14.103	−14.119	−14.108	96.33	96.35	96.33	96.34
11.5	−14.819	−14.811	−14.826	−14.816	95.08	95.10	95.08	95.09
12.0	−15.498	−15.490	−15.506	−15.495	93.95	93.96	93.94	93.96
12.5	−16.158	−16.150	−16.165	−16.154	92.90	92.91	92.90	92.91

Conclusion

A highly accurate mathematical model for the electromagnetic analysis of an inductive iris in a rectangular waveguide was developed and verified. By matching transverse field components, the electromagnetic wave reflection problem was reduced to two integral equations, which were subsequently solved by expanding the electric field in the aperture using basis functions. The correctness and precision of the model were validated by numerical simulations (FEM and FDTD) and experimental measurements of the reflection characteristics of two inductive irises in a standard rectangular waveguide.

Therefore, the developed mathematical model provides superior computational efficiency compared to full-wave numerical methods while maintaining excellent agreement with experimental data. The method presented in this article serves as a robust foundation for future research and the design of high-performance waveguide filters, diplexers, and polarizers based on conducting irises in both rectangular and square waveguides. Future investigations should focus on identifying the optimal basis functions that ensure the best accuracy and convergence for various iris geometries and thicknesses.

References

[1] Cai, H., Liu, H., Su, G., Yang, N., Liu, J. and Sun, L. (2023). A V-band wideband waveguide filters with inductive iris. *2023 16th UK-Europe-China Workshop on Millimetre Waves and Terahertz Technologies (UCMMT)*, pp. 1–3. DOI: 10.1109/UCMMT58116.2023.10310325.

[2] Kireeff Covo, M., Hassan, T., Duran, J. C., Lambert, K., Bloemhard, P. and Benitez, J. (2024). Inductive iris impedance matching network for a compact waveguide DC break. *IEEE Transactions on Microwave Theory and Techniques*, vol. 72, no. 12, pp. 6793–6798. DOI: 10.1109/TMTT.2024.3409470.

[3] Zhao, X., Glubokov, O., Campion, J., Gomez-Torrent, A., Krivovitca, A., Shah, U. and Oberhammer, J. (2020). Silicon micromachined D-band diplexer using releasable filling structure technique. *IEEE Transactions on Microwave Theory and Techniques*, vol. 68, no. 8, pp. 3448–3460. DOI: 10.1109/TMTT.2020.3004585.

[4] Campion, J., Glubokov, O., Gomez-Torrent, A., Krivovitca, A., Shah, U., Bolander, L., Li, Y. and Oberhammer, J. (2018). An ultra low-loss silicon-micromachined waveguide filter for D-band telecommunication applications. *2018 IEEE/MTT-S International Microwave Symposium - IMS*, pp. 583–586. DOI: 10.1109/MWSYM.2018.8439601.

[5] Mehrabi Gohari, M., Glubokov, O. and Oberhammer, J. (2025). Inline waveguide filters with transmission zeros using frequency-variant couplings. *IEEE Transactions on Microwave Theory and Techniques*, Vol. 73, Iss. 6, pp. 3310-3318. DOI: 10.1109/TMTT.2025.3541149.

[6] Bartlett, C., Glubokov, O., Kamrath, F. and Höft, M. (2023). Highly selective broadband mm-wave diplexer design. *IEEE Microwave and Wireless Technology Letters*, vol. 33, no. 2, pp. 149–152. DOI: 10.1109/LMWC.2022.3205425.

[7] Bulashenko, A. V., Piltyay, S. I., Kalinichenko, Y. I. and Zabegalov, I. V. (2021). Waveguide polarizer for radar and satellite systems. *Visnyk NTUU KPI Seriia – Radiotekhnika Radioaparatobuduvannia*, no. 86, pp. 5–13. DOI: 10.20535/RADAP.2021.86.5-13.

[8] Piltyay, S. (2021). Square waveguide polarizer with diagonally located irises for Ka-band antenna systems. *Advanced Electromagnetics*, vol. 10, no. 3, pp. 31–38. DOI: 10.7716/aem.v10i3.1780.

[9] Zhang, Y., Wang, Q. and Xin, H. (2014). A compact 3 dB E-plane waveguide directional coupler with full bandwidth. *IEEE Microwave and Wireless Components Letters*, vol. 24, no. 4, pp. 227–229. DOI: 10.1109/LMWC.2013.2296297.

[10] Hao, L., Zhang, B., Niu, Z., Li, D. and Liu, Y. (2025). A waveguide directional coupler with interleaved coupling holes. *2025 IEEE MTT-S International Microwave Workshop Series (IMWS-AMP)*, pp. 1–3. DOI: 10.1109/IMWS-AMP66175.2025.11136788.

[11] Fu, P.-H., Chao, C.-Y. and Huang, D.-W. (2021). Ultracompact silicon waveguide bends designed using a particle swarm optimization algorithm. *IEEE Photonics Journal*, vol. 13, no. 1, 6600509. DOI: 10.1109/JPHOT.2020.3043828.

[12] Prabha, P. U. K. and Raju, G. S. N. (2016). Analysis of L-band waveguide H-plane Tee junction. *2016 International Conference on ElectroMagnetic Interference & Compatibility (INCEMIC)*, pp. 1–4. DOI: 10.1109/INCEMIC.2016.7921485.

[13] Khorsandy, M., Salari, A., Pilevar, A. and Erricolo, D. (2019). An optimized broadband waveguide magic-T for X-band applications. *2019 PhotonIcs & Electromagnetics Research Symposium - Spring (PIERS-Spring)*, pp. 207–211. DOI: 10.1109/PIERS-Spring46901.2019.9017712.

[14] Piltyay, S., Bulashenko, A. and Shuliak, V. (2022). Development and optimization of microwave guide polarizers using equivalent network method. *Journal of Electromagnetic Waves and Applications*, vol. 36, no. 5, pp. 682–705. DOI: 10.1080/09205071.2021.1980913.

[15] Stutzman, W. L. (2018). *Polarization in electromagnetic systems*. Artech House, Norwood, 256 p.

[16] Virone, G., Tascone, R., Peverini, O. A., Addamo, G. and Orta, R. (2008). Combined-phase-shift waveguide polarizer. *IEEE Microwave and Wireless Components Letters*, vol. 18, no. 8, pp. 509–511. DOI: 10.1109/LMWC.2008.2001005.

[17] Tribak, A., Mediavilla, A., Cano, J. L., Boussouis, M. and Cepero, K. (2009). Ultra-broadband low axial ratio corrugated quad-ridge polarizer. *European Microwave Conference (EuMC)*, pp. 73–76. DOI: 10.23919/EUMC.2009.5295927.

[18] Güvenç, M., Şişman, I. and Ergin, A. A. (2023). Design and optimization of a wide-band quad-ridged polarizer for satellite communications. *2023 IEEE International Symposium on Antennas and Propagation and USNC-URSI Radio Science Meeting (USNC-URSI)*, pp. 1477–1478. DOI: 10.1109/USNC-URSI52151.2023.10237410.

[19] Polo-Lopez, L., Masa-Campos, J. L. and Ruiz-Cruz, J. A. (2017). Design of a reconfigurable rectangular waveguide phase shifter with metallic posts. *2017 47th European Microwave Conference (EuMC)*. DOI: 10.23919/EuMC.2017.8231036.

[20] Deutschmann, B. and Jacob, A. F. (2020). Broadband septum polarizer with triangular common port. *IEEE Transactions on Microwave Theory and Techniques*, vol. 68, no. 2, pp. 693–700. DOI: 10.1109/TMTT.2019.2951138.

[21] Güvenç, M., Şişman, I. and Ergin, A. A. (2023). Design, optimization and fabrication of a X-band septum polarizer for satellite communication. *2023 IEEE International Symposium on Antennas and Propagation (USNC-URSI)*, pp. 1347–1348. DOI: 10.1109/USNC-URSI52151.2023.10237446.

[22] Kirilenko, A., Mospan, L. and Tkachenko, V. (2002). Extracted pole bandpass filters based on the slotted irises. *2002 32nd European Microwave Conference*, pp. 1–4. DOI: 10.1109/EUMA.2002.339448.

[23] Deng, C., Zhang, R. and Fan, X. (2016). V-band waveguide band-pass filter with tuning screws. *2016 IEEE International Conference on Microwave and Millimeter Wave Technology (ICMMT)*, pp. 416–418. DOI: 10.1109/ICMMT.2016.7761793.

[24] Peverini, O. A., Virone, G., Addamo, G. and Tascone, R. (2011). Development of passive microwave antenna-feed systems for wide-band dual-polarisation receivers. *IET Microwaves, Antennas & Propagation*, vol. 5, no. 8, pp. 1008–1015. DOI: 10.1049/iet-map.2010.0340.

[25] Kirilenko, A., Mospan, L. and Steshenko, S. (2018). A way to realize a multi-frequency polarization plane rotator. *2018 9th International Conference on Ultrawideband and Ultrashort Impulse Signals (UWBUSIS)*, pp. 218–221. DOI: 10.1109/UWBUSIS.2018.8520246.

[26] Kirilenko, A. A., Steshenko, S. O., Derkach, V. N. and Ostryzhnyi, Y. M. (2019). A tunable compact polarizer in a circular waveguide. *IEEE Transactions on Microwave Theory and Techniques*, vol. 67, no. 2, pp. 592–596. DOI: 10.1109/TMTT.2018.2881089.

[27] Kirilenko, A., Steshenko, S. and Ostryzhnyi, Y. (2024). Compact filter-rotator of polarization plane with uniform angular response. *Radioelectronics and Communications Systems*, vol. 67, pp. 258–264. DOI: 10.3103/S0735272724050054.

[28] Meixner, J. (1972). The behavior of electromagnetic fields at edges. *IEEE Transactions on Antennas and Propagation*, vol. 20, no. 4, pp. 442–446. DOI: 10.1109/TAP.1972.1140243.

[29] Marchetti, S. and Rozzi, T. (1991). Electric field singularities at sharp edges of planar conductors. *IEEE Transactions on Antennas and Propagation*, vol. 39, no. 9, pp. 1312–1320. DOI: 10.1109/8.99039.

[30] Krähenbühl, L., Buret, F., Perrussel, R., Voyer, D., Nicolas, P. and Nicolas, L. (2011). Numerical treatment of rounded and sharp corners in the modeling of 2D electrostatic fields. *Journal of Microwaves, Optoelectronics and Electromagnetic Applications*, vol. 10, no. 1, pp. 66–81. DOI: 10.1590/S2179-10742011000100008.

[31] Martyniuk, S. Y., Dubrovka, F. F., Zakharchenko, O. S. and Stepanenko, P. Y. (2021). Effective high-precision analysis of thin asymmetric inductive diaphragm in rectangular waveguide using integral equation method. *Radioelectronics and Communications Systems*, vol. 64, pp. 80–91. DOI: 10.3103/S0735272721020035.

[32] Reimer, M. (2003). *Gegenbauer polynomials*. In *Multivariate polynomial approximation* (pp. 19–20). Birkhäuser, Basel. DOI: 10.1007/978-3-0348-8095-4_2.

[33] Gradshteyn, I. S. and Ryzhik, I. M. (2014). *Table of integrals, series, and products* (8th ed.). Academic Press, 1133 p. DOI: 10.1016/C2010-0-64839-5.

[34] Jin, J.-M. (2014). *The finite element method in electromagnetics* (3rd ed.). Wiley-IEEE Press, 876 p. DOI: 10.1002/9781119127505.

[35] Piltyay, S. I., Bulashenko, A. V. and Herhil, Y. Y. (2021). Numerical performance of FEM and FDTD methods for the simulation of waveguide polarizers. *Visnyk NTUU KPI Seriia – Radiotekhnika Radioaparatobuduvannia*, no. 84, pp. 11–21. DOI: 10.20535/RADAP.2021.84.11-21.

Електродинамічний аналіз індуктивної діафрагми у прямокутному хвилеводі гібридним методом узгодження мод та інтегральних рівнянь

Пільтяй С. І.

Індуктивні діафрагми застосовують у сучасних мікрохвильових фільтрах, диплексерах, поляризаторах і ротаторах на основі хвилеводів. У статті представлено ефективний математичний метод аналізу характеристик електромагнітних хвиль, що розсіюються на індуктивній діафрагмі у прямокутному хвилеводі. За допомогою методу узгодження поперечних компонент поля задачу розсіювання електромагнітних хвиль зведено до системи зв'язаних інтегральних рівнянь, яку перетворено на нову систему розділених (незалежних) рівнянь. Кожне рівняння розв'язано шляхом розкладання електричного поля у вікні діафрагми у ряд за базисними функціями. Цю процедуру реалізовано з використанням систем ортогональних тригонометричних базисних функцій поля апертури, ортогональних базисних функцій на основі поліномів Гегенбауера з ваговою функцією з показником степеня 1/2 або ортогональних базисних функцій на основі поліномів Гегенбауера з ваговою функцією з показником степеня 2/3. У результаті визначено комплексні амплітуди всіх мод у кожній області внутрішнього об'єму (до діафрагми, всередині її вікна та після діафрагми), а також комплексні коефіцієнти відбиття та передачі основної хвилі H_{10}.

Для перевірки достовірності та точності розробленої математичної моделі проведено додаткові розрахунки числовими методами: методом скінченних елементів (FEM) та методом скінченних різниць у часовій області (FDTD), а також експериментальні вимірювання характеристик відбиття для двох індуктивних діафрагм у стандартному прямокутному хвилеводі. Вимірювальні установки включали скалярний або векторний аналізатори кіл (панорамні вимірювачі), одну з двох індуктивних діафрагм, узгоджене навантаження та хвилевідні тракти. Експериментально отримані коефіцієнти відбиття добре узгоджуються з результатами, передбаченими розробленою математичною моделлю та числовими методами.

Розроблена математична модель може бути широко застосована для аналізу характеристик електромагнітних хвиль, які розсіюються на індуктивних діафрагмах у хвилеводах, та для синтезу різноманітних мікрохвильових пристроїв на їх основі.

Ключові слова: електродинамічний аналіз; моделювання електромагнітних полів; метод узгодження мод; інтегральні рівняння; індуктивні діафрагми; прямокутний хвилевід; розподіл поля; базисні функції; поліноми Гегенбауера; хвилевідні компоненти